

# Interferometric CO(3–2) Observations toward the Central Region of NGC 1068

Mengchun Tsai<sup>1</sup>, Chong-Yuan Hwang<sup>1</sup>, Satoki Matsushita<sup>2,3</sup>, Andrew J. Baker<sup>4</sup>, Daniel  
Espada<sup>5,6,2</sup>

Received \_\_\_\_\_; accepted \_\_\_\_\_

---

<sup>1</sup>Institute of Astronomy, National Central University, Taiwan, R.O.C.

<sup>2</sup>Academia Sinica Institute of Astronomy and Astrophysics, P.O. Box 23-141, Taipei  
10617, Taiwan, R.O.C.

<sup>3</sup>Academia Sinica Institute of Astronomy and Astrophysics, Joint ALMA Office, Av. El  
Golf 40, Piso 18, Las Condes, Santiago, Chile

<sup>4</sup>Department of Physics and Astronomy, Rutgers, the State University of New Jersey, 136  
Frelinghuysen Road, Piscataway, NJ 08854

<sup>5</sup>Instituto de Astrofísica de Andalucía - CSIC, Apdo. 3004, 18080 Granada, Spain

<sup>6</sup>Harvard-Smithsonian Center for Astrophysics, 60 Garden St., Cambridge, MA 02138

## ABSTRACT

We present CO(3–2) interferometric observations of the central region of the Seyfert 2 galaxy NGC 1068 using the Submillimeter Array, together with CO(1–0) data taken with the Owens Valley Radio Observatory Millimeter Array. Both the CO(3–2) and CO(1–0) emission lines are mainly distributed within  $\sim 5$  arcsec of the nucleus and along the spiral arms, but the intensity distributions show differences; the CO(3–2) map peaks in the nucleus, while the CO(1–0) emission is mainly located along the spiral arms. The CO(3–2)/CO(1–0) ratio is about 3.1 in the nucleus, which is four times as large as the average line ratio in the spiral arms, suggesting that the molecular gas there must be affected by the radiation arising from the AGN. On the other hand, the line ratios in the spiral arms vary over a wide range from 0.24 to 2.34 with a average value around 0.75, which is similar to the line ratios of star-formation regions, indicating that the molecular gas is affected by star formation. Besides, we see a tight correlation between CO(3–2)/(1–0) ratios in the spiral arms and star formation rate surface densities derived from *Spitzer* 8  $\mu\text{m}$  dust flux densities. We also compare the CO(3–2)/(1–0) ratio and the star formation rate at different positions within the spiral arms; both are found to decrease as the radius from the nucleus increases.

*Subject headings:* galaxies: active, galaxies: individual (NGC 1068), galaxies: ISM, galaxies: nuclei, galaxies: Seyfert

## 1. INTRODUCTION

The properties of circumnuclear molecular gas (CMG) near an active galactic nucleus (AGN) can be influenced by the AGN itself. Some CMG observations of Seyfert galaxies with a spatial resolution around 100 to 300 pc have shown that the intensities of CO(2–1) line emission are about two times higher in temperature units than those of CO(1–0) emission (e.g., Matsushita et al. 2004; Hsieh et al. 2008). This is different from the properties of molecular clouds in normal or star-forming galaxies, which usually show brightness temperatures in higher-J transitions similar to or lower than those in lower-J lines (e.g., Devereux et al. 1994; Mauersberger et al. 1999; Dumke et al. 2001; Oka et al. 2007; Matsushita et al. 2009). From the LVG model, the high values of CO(2–1)/CO(1–0) arise when the emitting molecular gas is in a low opacity environment and the resulting molecular densities are larger than the critical densities of CO(1–0) and CO(2–1) transitions. A possible origin for such unusual behavior is that CMG near AGNs traces X-ray dominated regions due to the strong radiation (e.g., Maloney et al. 1996; Kohno et al. 2001; Usero et al. 2004; Meijerink & Spaans 2005; Meijerink et al. 2007). Unlike far-UV photons, X-ray photons have greater penetration lengths and are more efficient in gas heating (Usero et al. 2004). On the other hand, CMG can also be affected by mechanical processes, such as gas entrainment by jets (Matsushita et al. 2007).

Star formation in galaxies is well correlated with gas surface density as embodied in the famous Schmidt-Kennicutt law (Schmidt 1959; Kennicutt 1998). In the circumnuclear regions (CNRs) and inner structures of galaxies, the molecular gas usually has relatively higher densities and temperatures than the molecular gas in galaxy disks; in such environments, star formation is expected to be much more vigorous (Kennicutt 1998; Tan 2000). Krumholz & Thompson (2007) suggest that the Schmidt-Kennicutt law might change slope when the averaged gas density is close to the line critical density. We note that

the critical densities of CO(1–0) ( $\sim 10^3 \text{ cm}^{-3}$ ) and CO(3–2)  $\sim 3 \times 10^4 \text{ cm}^{-3}$  are comparable with the densities of the CNRs of some nearby active galaxies, which are around 300 to  $10^7 \text{ cm}^{-3}$  (e.g., Matsushita et al. 2004; Sakamoto et al. 2007; Pérez-Beaupuits et al. 2009). It is unclear whether or how the Schmidt-Kennicutt law would vary in the CNRs of these galaxies when probed with CO(1–0) and CO(3–2) emission.

Among nearby galaxies, NGC 1068 is the best-studied prototypical Seyfert. It has a distance of 14.4 Mpc (Tully 1988, ;  $1'' \sim 70 \text{ pc}$ ) and is classified as (R)SA(rs)b in the RC3 catalog (de Vaucouleurs et al. 1991), with an inner bar in the central kpc and two tightly wound spiral arms starting from the tip of the bar (Scoville et al. 1988; Thronson et al. 1989). The inner 2 kpc is rich in star formation (Telesco et al. 1984), and the active star forming regions are concentrated along the spiral arms (e.g., Telesco & Decher 1988; Davies et al. 1998; Emsellem et al. 2006). Molecular gas is also abundant along the spiral arms (e.g., Myers & Scoville 1987; Planesas et al. 1991; Kaneko et al. 1992; Helfer & Blitz 1995), and a weak offset ridge of emission along the leading side of the bar is also seen (Helfer & Blitz 1995; Schinnerer et al. 2000), which is a typical molecular gas distribution in barred galaxies.

The nucleus of NGC 1068 shows radio jets (e.g., Wilson & Ulvestad 1983; Gallimore et al. 1996, 2004) and an ionization cone (e.g., Pogge 1988; Macchetto et al. 1994). The nuclear optical spectrum has type 2 characteristics, but the polarized spectrum shows type 1 features, reflecting the existence of an optically thick torus or disk around the central massive black hole (Antonucci & Miller 1985). Indeed, a sub-parsec scale ionized gas disk perpendicular to the radio jets has been observed (Gallimore et al. 1997, 2004), with a molecular gas (maser) torus (Greenhill et al. 1996) or disk (Gallimore et al. 2001) located outside of the ionized gas disk. This maser torus/disk may be surrounded by a pc-scale warm dust torus (Jaffe et al. 2004). Outside this structure, the existence of a warped

molecular gas disk is suggested by interferometric CO(2–1) observations (Baker & Scoville 1998; Schinnerer et al. 2000), but warm molecular gas kinematics dominated by irregular (infalling) motions have been observed in 2.12  $\mu\text{m}$  1–0 S(1) molecular hydrogen emission (Müller Sánchez et al. 2009). Interferometric observations of molecular gas emission with angular resolutions at 0."5–2" also indicated non-circular motions in the central  $\sim 100$  pc (Krips et al. 2011). The intensity ratios of various molecular species exhibit peculiar values, including very high HCN/CO and HCN/HCO<sup>+</sup> ratios (Jackson et al. 1993; Tacconi et al. 1994; Kohno et al. 2001; Usero et al. 2004; Krips et al. 2008; Pérez-Beaupuits et al. 2009), suggesting that the molecular gas very close to the Seyfert 2 nucleus is irradiated by strong X-ray emission (Usero et al. 2004; Kohno 2005; Kohno et al. 2008; Garcia-Burillo et al. 2010).

The central region of NGC 1068 has been mapped in different CO transition lines by both single-dish and interferometric observations. Among the former, it has been observed by Scoville et al. (1983, CO(1–0), FCRAO), Kaneko et al. (1989, CO(1–0), Nobeyama), Planesas et al. (1989, CO(1–0) and CO(2–1), IRAM), Young et al. (1995, CO(1–0), FCRAO), Papadopoulos & Seaquist (1999, CO(2–1) and CO(3–2), JCMT), and Israel (2009, CO(1–0), CO(2–1), CO(3–2), and CO(4–3), IRAM and JCMT). With interferometers, it has been observed by Planesas et al. (1991, CO(1–0), OVRO), Kaneko et al. (1992, CO(1–0), NMA), Helfer & Blitz (1995, CO(1–0), BIMA), Schinnerer et al. (2000, CO(1–0) and CO(2–1), IRAM), Helfer et al. (2003, CO(1–0), BIMA), and Krips et al. (2011, CO(2–1) and CO(3–2), SMA/PdBI). In this paper, we present interferometric observations of the CO(3–2) line in the central 2 kpc of NGC 1068 using the Submillimeter Array (SMA). We also show interferometric observations of the CO(1–0) transition, with  $uv$  sampling similar to that of the CO(3–2) data, from the Owens Valley Radio Observatory (OVRO) Millimeter Array. We describe our observations in Sect. 2 and show the overall molecular gas distributions in Sect. 3. Line ratios, molecular gas masses, and kinematics are presented

and discussed in Sect. 4.1, 4.2, and 4.3, respectively. The relation between line ratios and star formation is discussed in Sect. 4.4, and a summary is in Sect. 5.

## 2. OBSERVATIONS AND DATA REDUCTION

### 2.1. SMA CO(3–2) Observations

We used the SMA to acquire three CO(3–2) datasets on August 13, 15, and 23, 2005. The zenith opacity at 225 GHz was about 0.07 in August 13 and 15 and 0.06 in August 23. Six out of eight 6-m antennas were used in the compact configuration. The receivers were tuned to the redshifted CO(3–2) line (344.493 GHz). Correlators were set to cover a velocity range of  $\sim 1700 \text{ km s}^{-1}$  ( $\sim 2 \text{ GHz}$  bandwidth) and configured to have a velocity resolution of  $\sim 0.7 \text{ km s}^{-1}$  ( $= 0.8125 \text{ MHz}$  frequency resolution). The SMA antenna primary beam has a half power beam width (HPBW) of  $\sim 36''$  ( $\sim 2.5 \text{ kpc}$  in NGC 1068) at 345 GHz. A 7-pointing mosaic (pointings separated by  $18''$  and hexagonal in shape) was observed in order to image the inner  $72''$  ( $5 \text{ kpc}$ ) of NGC 1068. The phase center was set at R.A. =  $2^{\text{h}}42^{\text{m}}40.798^{\text{s}}$  and decl. =  $-0^{\circ}00^{\text{m}}47.938^{\text{s}}$  (J2000), corresponding to the AGN position (Muxlow et al. 1996).

We performed the data reduction following the standard processes outlined in the SMA cookbook<sup>1</sup>. The visibilities were first calibrated with the IDL-based MIR package (Scoville et al. 1993) as modified for the SMA. We used 0423 – 013 as the amplitude and phase calibrator to track phase and gain variations and used 3C 454.3 for bandpass and flux calibrations.

We calibrated our observations by linearly interpolating the flux densities of the quasar

---

<sup>1</sup><http://cfa-www.harvard.edu/~cqi/mircook.html>

3C 454.3, which were  $26.48 \pm 1.33$  Jy on August 12 and  $18.90 \pm 0.95$  Jy on August 25, according to the SMA calibrator list<sup>2</sup>. The expected flux densities of 3C 454.3 were about  $25 \pm 1.3$  (August 13-15), and  $20 \pm 1.0$  (August 23) during the observations. Mars and Uranus were also observed during the observations. However, Mars was resolved by the SMA observations, and Uranus was only observed on August 13 and 15. After performing the flux calibration with 3C 454.3, we compared the fluxes of Uranus and Mars to check the accuracy of our flux calibration. The uncertainty in our flux scale is estimated to be  $\sim 10\%$ .

We combined the visibilities from all the mosaic observations and applied the mapping task INVERT in MIRIAD to produce “dirty” images with a velocity resolution of  $10 \text{ km s}^{-1}$ . Primary beam correction was taken into account in the mosaic mode of the INVERT process. We used natural weighting in the mapping process in order to have the best sensitivity. We deconvolved the dirty images with the MOSSDI and MOSMEM packages in MIRIAD, and produced moment maps and spectra for further analysis. The resulting spatial resolution was  $2''.29 \times 2''.00$  ( $\sim 160 \times 140 \text{ pc}^2$ ) with a position angle of  $-88^\circ.8$ .

## 2.2. OVRO CO(1–0) Observations

We observed the CO(1–0) transition in NGC 1068 (adopted pointing center:  $\alpha_{\text{J2000}} = 02:42:40.7$  and  $\delta_{\text{J2000}} = -00:00:47.7$ ) between April and September 1995 using the OVRO millimeter array (Padin et al. 1991; Scott & Finch 1993). The array comprised six 10.4 m antennas, which during our observations were deployed in three configurations providing a total of 40 distinct baselines. We configured the array’s digital correlator (Padin et al. 1993) to provide 112 contiguous frequency channels, each Hanning-smoothed to 4 MHz ( $10.4 \text{ km s}^{-1}$ ) resolution. We calibrated the data within the OVRO millimeter array

---

<sup>2</sup><http://sma1.sma.hawaii.edu/callist/callist.html>

database using the MMA package (Scoville et al. 1993). Paired integrations on J0339–017, interleaved with observations of NGC 1068 every 30–40 minutes, were used to correct for phase and gain variations; for passband calibration, we used 3C273, 3C454.3, and/or 0528+134. Our flux scale was determined by comparing J0339–017 with Uranus or Neptune in light of standard brightness temperature models for the latter (Muehleman & Berge 1991; Orton et al. 1986), or by bootstrapping from archived observations of the planets (and bright, frequently-observed quasars) obtained with similar elevations and coherences. From repeatability of flux measurements on 1–2 week timescales, we estimate that the uncertainty in our flux scale is  $\sim 10\%$ .

After editing for quality in the Difmap package (Shepherd 1997), we were left with 11.4 hours of on-source data. To eliminate contamination by 3 mm continuum emission associated with NGC 1068’s jet, we subtracted a  $uv$ -plane model based on the line-free channels at the ends of the recorded bandwidth. The line-free  $uv$  data were then mapped using the IMAGR task in the NRAO AIPS package, with moderately robust weighting giving a synthesized beam of  $3''.46 \times 2''.56$  ( $242 \text{ pc} \times 179 \text{ pc}$ ) at PA  $67^\circ 5$ . For deconvolution, we adopted a single clean box for all channels that enclosed all of the emission in the zeroth moment map. A slightly different reduction of these data was first discussed by Baker & Scoville (1998). Before analyzing moment maps and spectra, we applied a primary beam correction appropriate for the  $\sim 56''$  OVRO HPBW.

### 3. CO Distribution

In Figure 1, we show the integrated intensity and velocity maps of the CO(3–2) line for the central region of NGC 1068. CO(3–2) emission appears in the nucleus and along the two spiral arms. The CO(3–2) distribution in the nucleus is elongated in an east-west direction, and the strongest peak in our data is located  $\sim 1''$  east of the nucleus. The distribution

of the CO(3–2) emission is roughly consistent with that of previous CO(1–0) observations (e.g., Helfer & Blitz 1995; Planesas et al. 1991; Kaneko et al. 1992; Schinnerer et al. 2000) except that the nucleus is relatively brighter in the CO(3–2) image.

The CO(3–2) intensity distributions in the two spiral arms are different. The southern arm is brighter than the northern arm. The second strongest peak in our map is located  $\sim 12''$  south of the nucleus, which is on the southern arm. The locations of these two strongest peaks in the map can explain the position of the peak intensity in an early CO(3–2) single-dish image (Papadopoulos & Seaquist 1999), which showed a peak intensity offset south of the nucleus. The missing flux in the central  $14''$  region is about 20% when comparing our image with a JCMT observation of the central region of NGC 1068 (Israel 2009). On the other hand, if we compare our data with an area-averaged CO(3–2) spectrum over a circular area of  $30''$  radius (Papadopoulos & Seaquist 1999), we find that our map only recovers  $\sim 50\%$  of the total flux. The missing flux might seem surprisingly large; however, Papadopoulos & Seaquist (1999) have showed that the total CO(3–2) flux is actually dominated by a warm diffuse gas phase, which is highly excited and not virialized. Besides, similar extended structures of CO(3–2) emission are also observed in the central regions of other nearby AGNs, such as M51 (Matsushita et al. 2004). Most of this diffuse gas is likely resolved out and not detectable in our interferometer map.

The CO(1–0) integrated intensity and velocity maps are shown in Figure 2. As in the CO(3–2) map, CO(1–0) emission is located in the nucleus and along the two spiral arms, but the strongest peak is located at the southern arm, and the peak intensity at the core region is relatively weak. Our CO(1–0) image is in general agreement with previous interferometric CO(1–0) observations (Planesas et al. 1991; Kaneko et al. 1992; Schinnerer et al. 2000; Helfer et al. 2003). However, the BIMA image seems to show more emission at interarm regions. The difference between our results and the BIMA image might be due to the fact

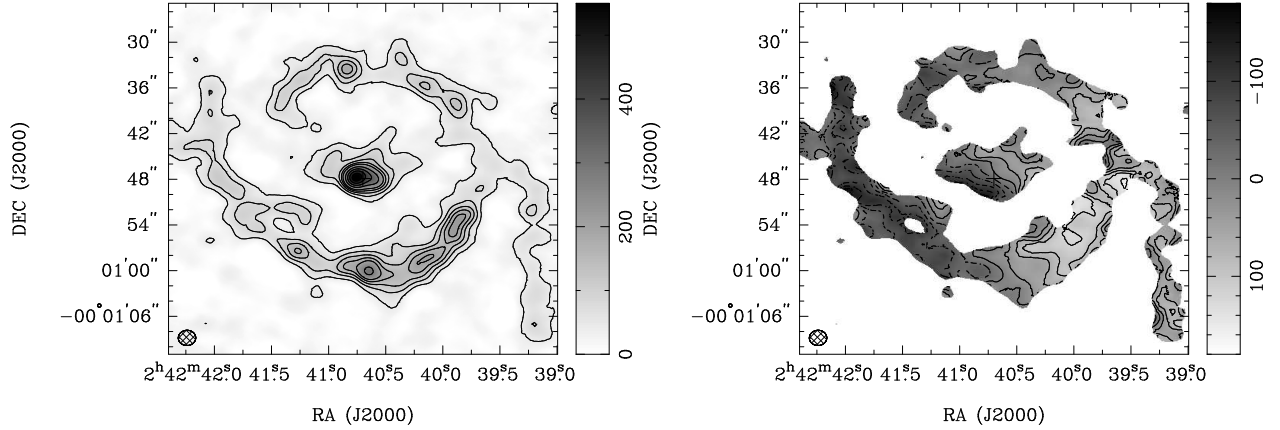


Fig. 1.— *Left*: CO(3–2) integrated intensity (moment 0) map of the central region of NGC 1068. The grayscale range is shown in the wedge at right in units of  $\text{Jy beam}^{-1} \text{ km s}^{-1}$ . The contour levels are 10, 20, 30, 40, 50, 70, 90, 110, and  $130 \times \sigma$ , where  $1\sigma = 4.0 \text{ Jy beam}^{-1} \text{ km s}^{-1}$ . The synthesized beam is  $2''.29 \times 2''.00$  ( $\sim 160 \times 140 \text{ pc}^2$ ) with a P.A. of  $-88^\circ.0$ , which is shown in the bottom left corner. The cross indicates the galactic center determined from the 5 GHz and 22 GHz radio continuum data (Muxlow et al. 1996). *Right*: CO(3–2) intensity-weighted velocity field (moment 1) map. The grayscale range is shown in the wedge at right from -180 to 180  $\text{km s}^{-1}$ . The contour levels range from  $-150$  to  $+150 \text{ km s}^{-1}$  with a  $30 \text{ km s}^{-1}$  interval.

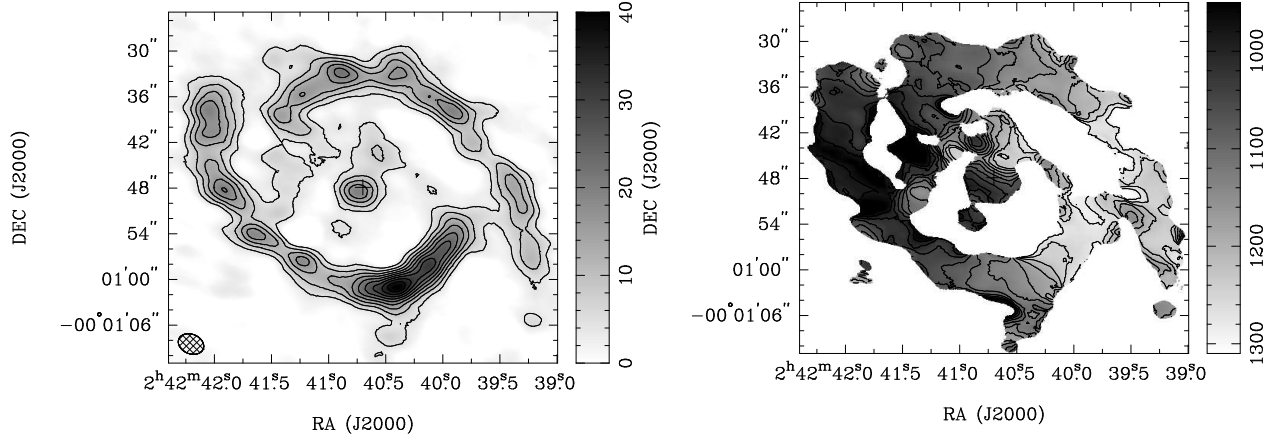


Fig. 2.— *Left*: CO(1–0) integrated intensity (moment 0) map of the central region of NGC 1068. The grayscale range is shown in the wedge at right in units of  $\text{Jy beam}^{-1} \text{ km s}^{-1}$ . The contour levels are multiplies of  $5\sigma$ , where  $1\sigma = 0.81 \text{ Jy beam}^{-1} \text{ km s}^{-1}$ . The synthesized beam is  $3''.46 \times 2''.56$  with a P.A. of  $67^\circ.5$ , which is shown in the bottom left corner. The cross is the same as in Fig. 2. *Right*: CO(1–0) intensity weighted velocity field (moment 1) map of the central region of NGC 1068. The grayscale range is shown in the wedge at the right, from  $-180$  to  $180 \text{ km s}^{-1}$ . The contour levels range from  $-150$  to  $+150 \text{ km s}^{-1}$  with a  $30 \text{ km s}^{-1}$  interval.

that the BIMA image have included modelled visibilities derived from single-dish NRAO observations and might contain large-scale emission that would be resolved out by our interferometric observations.

The corresponding missing flux of CO(1–0) in the core region is about 20% comparing with the BIMA results of Helfer et al. (2003). For the spiral regions, the situation is more complicated. We have estimated the missing fluxes for several selected spiral regions (see Figure 3) and obtained diverse results. For example, the missing flux for R4 is about 70% and for R17 is about 38%; however, we detect more flux than BIMA for R15, so there should be no missing flux for R15. We note that R4 is an inter-arm region, which is dominated by diffuse emission, while R15 is around a compact structure peak and R17 is at the boundary of an arm structure. These different results might be caused by different  $uv$  coverage of the BIMA and our observations.

The overall CO(1–0) velocity field is similar to that of CO(3–2). Both have a rotation axis with P.A. about  $-30^\circ$  and a rotation velocity of  $120 \text{ km s}^{-1}$  in the nucleus. In the spiral arms, both kinematic major axes run from east to west with a rotation velocity of  $180 \text{ km s}^{-1}$ .

## 4. Discussion

### 4.1. CO Line Ratios

Before deriving line ratios at various regions, we first matched the  $uv$  range between our CO(3–2) and CO(1–0) datasets. In Figure 3, we overlay the CO(3–2) (solid contours) and CO(1–0) (dashed contours) intensity distributions. In this image, the shortest  $uv$  length is set to  $16 \text{ k}\lambda$ , and the image resolutions are convolved into the same resolution ( $3''.46 \times 2''.56$  with a P.A. of  $67^\circ 5$ ). As mentioned above, the overall distributions of both CO(3–2) and

CO(1–0) are very similar, but some of the intensity peaks have shifted positions with respect to each other. The most obvious example is in the southern spiral arm, about  $12'' - 14''$  south of the nucleus, where the CO(3–2) peak is located in the inner part of the spiral arm, but the CO(1–0) peak is shifted toward the outer edge of the spiral arm.

We divide the central region of NGC 1068 into 25 regions covering the nucleus and spiral arms, as shown in Figure 3 (C1 and R1 – R24). The size of each region is  $4'' \times 5''$  except C1, which is  $6'' \times 5''$ . The intensity scale is then converted to a brightness temperature scale, and the CO(3–2)/CO(1–0) brightness temperature ratios,  $R_{31}$ , are derived for each region using the MIRIAD task MATHS. Area-averaged spectral peak and integrated brightness temperatures and  $R_{31}$  for each region are shown in Table 1.

The central core region C1 exhibits a very high integrated intensity ratio with  $R_{31} = 3.12 \pm 0.03$  and a spectra peak ratio of  $2.83 \pm 0.10$ . Figure 4 shows the spectra of C1. The CO(3–2)/CO(1–0) line ratio is slightly smaller than the results of Krips et al. (2011), which are about 4–6. However, the observations of Krips et al. (2011) have a much higher angular resolution and might contain relatively more contribution from the circumnuclear region of the AGN, while our result is an average value over a much larger area and are likely to include emission from outside regions. In fact, if we only consider the line ratio within the brightest beam at the center, we would obtain a line ratio of  $\sim 4.6$ , which is similar to the results of Krips et al. (2011).

On the other hand, the spiral arm regions R1 – R24 have a wide range of integrated intensity ratios of 0.24 – 2.34 and an average value of 0.75 with standard deviation 0.47. We note that the wide range of the intensity ratios might be caused by the different spatial distributions of the CO(1–0) and CO(3–2) emission due to varying physical conditions of the molecular gas. There is no obvious ratio difference between the northern and southern arms; the average ratio of the northern arm regions (R1 – R4, R18 – R24) is 0.8 and that

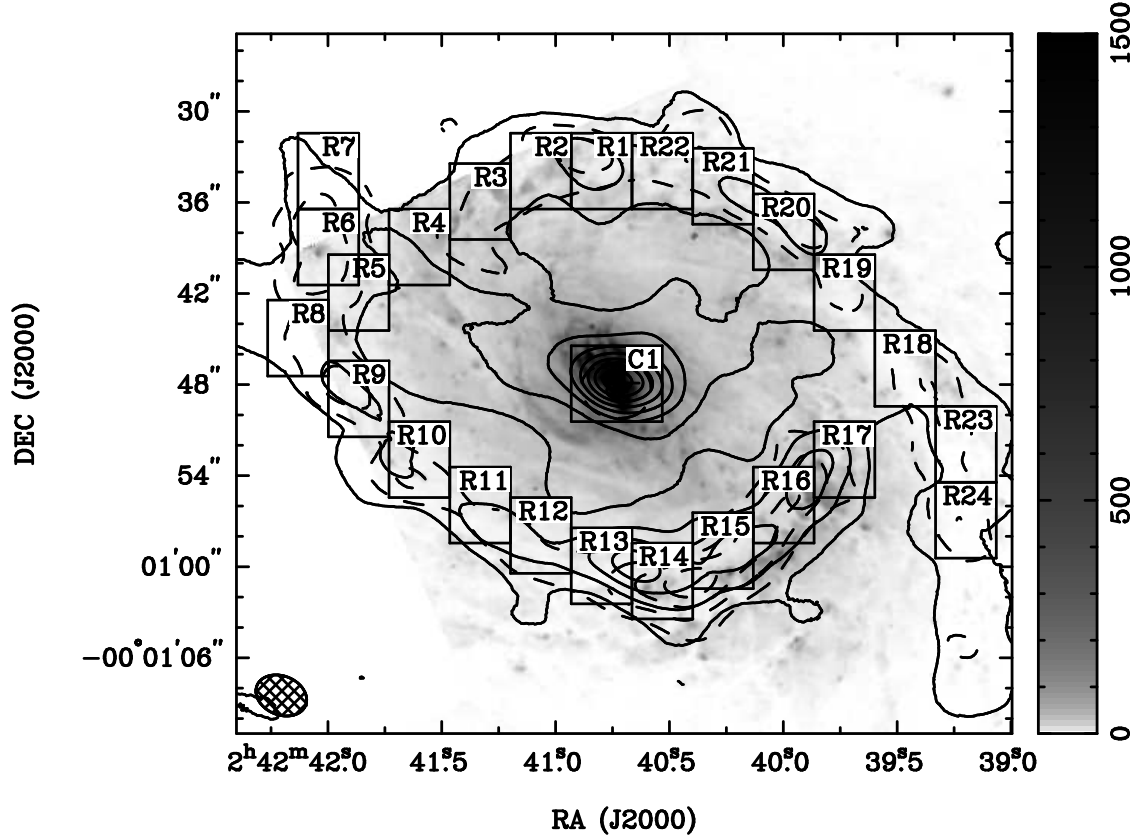


Fig. 3.— Integrated intensity maps of CO(3–2) (solid contours) and CO(1–0) (dashed contours), overlaid on the continuum-subtracted *HST* F658N image (greyscale) of the central region of NGC 1068. Solid contour levels for CO(3–2) are 10, 30, 50, 70, 90, 110, and  $130 \times 5.3 \text{ Jy beam}^{-1} \text{ km s}^{-1}$ , and dashed contour levels for CO(1–0) are 2, 4, 6,  $8 \times 5 \text{ Jy beam}^{-1} \text{ km s}^{-1}$ . The CO(3–2) and CO(1–0) data are matched to the same  $uv$  range and have the same synthesized beam size of  $3''.46 \times 2''.56$  ( $\sim 242 \times 179 \text{ pc}^2$ ) with a P.A. of  $67^\circ.5$ , which is shown in the bottom-left corner of the image. Cross is the same as in Figure 1. We also plot 25 boxes (C1 and R1 – R24) that are used to calculate the line ratios.

of the southern arm regions (R5 – R17) is 0.7. However, there is a difference between inner arm regions and outer arm regions; the average ratio of the inner arm regions (R1 – R4, R9 – R17, and R19 – R22) is  $0.88 \pm 0.14$ , while the outer arm regions (R5 – R8, R18, R23, and R24) show  $0.42 \pm 0.05$ . This difference indicates that there is a large-scale gradual decrease of the line intensity ratio from the inner radii to the outer radii. The radial change of molecular line ratios, and therefore of the physical conditions of the molecular gas, has also been detected in the Milky Way and other galaxies (Turner 1993; Aalto et al. 1994; Sakamoto 1994; Sakamoto et al. 1997; Petitpas & Wilson 2000; Paglione et al. 2001; Matsushita et al. 2010), suggesting that this trend is common.

The line ratios  $R_{31}$  in the spiral arm regions are similar to those observed in the centers of nearby normal and starburst galaxies. Devereux et al. (1994) observed seven nearby starburst galaxies and found that the ratios are in the range of 0.5 – 1.4 with an average ratio of  $0.64 \pm 0.06$ . A survey toward the centers of 28 nearby star-forming galaxies showed that most of their  $R_{31}$  are within the range of 0.2 – 0.7 (Mauersberger et al. 1999). On the other hand, the value of  $R_{31}$  in the nucleus is much larger than those observed in the nuclei of the nearby galaxies mentioned above, albeit similar to that observed in the nucleus of the Seyfert 2 galaxy M51. The inner  $uv$ -truncated  $R_{31}$  of the central molecular core of M51 also has a very high value of  $\sim 5.2 \pm 1.7$  within a beam size of  $3''.9 \times 2''.6$  or  $160 \text{ pc} \times 110 \text{ pc}$  (missing flux corrected  $R_{31}$  is  $\geq 1.9 \pm 0.2$ ; Matsushita et al. 2004). If we only correct the 20% missing flux of the CO(1–0) emission in the core region of NGC 1068 and ignore the missing flux of the CO(3–2) following the method of Matsushita et al. (2004), the  $R_{31}$  ratio of the core region will become 2.50 instead of 3.12. This suggests that the physical conditions of molecular gas around the Seyfert 2 AGN in NGC 1068 are very different from those in the centers of nearby star-forming and starburst galaxies, but might be similar to those around the Seyfert 2 nucleus of M51.

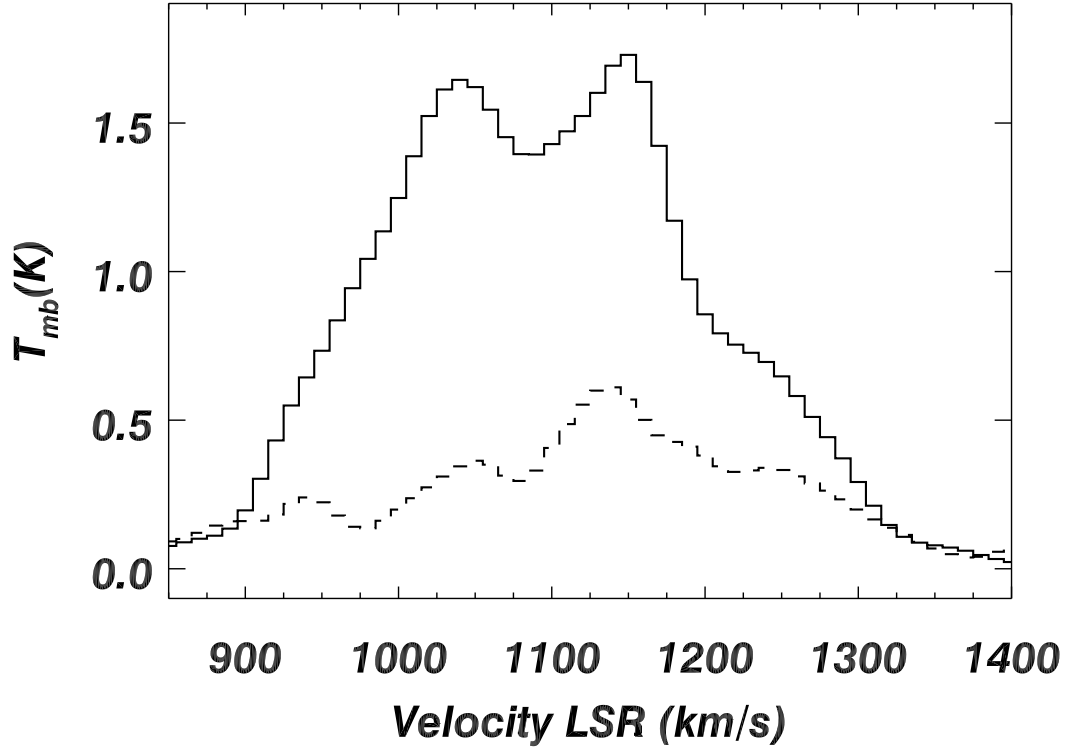


Fig. 4.— Area-averaged spectra within the C1 region. The solid line shows the spectrum of CO(3–2), and the dash line shows the spectrum of CO(1–0). The uncertainties per channel are about 0.01 K for the CO(3–2) spectrum and 0.02 K for the CO(1–0) one.

Table 1. Peak and integrated brightness temperature of CO(3–2) and CO(1–0), and the CO(3–2)/CO(1–0) line ratios, in different areas.

Area	Peak CO(3–2) [K]	Peak CO(1–0) [K]	Peak $R_{31}$	$\int T_B(\text{CO } J = 3 - 2) dv$ [K km s <sup>–1</sup> ]	$\int T_B(\text{CO } J = 1 - 0) dv$ [K km s <sup>–1</sup> ]	$R_{31}$	X offset [arcsec]	Y offset [arcsec]
C1	1.73 ± 0.01	0.61 ± 0.03	2.83 ± 0.10	438.5 ± 0.7	140.6 ± 1.5	3.12 ± 0.03	-1	0
R1	1.80 ± 0.03	1.55 ± 0.06	1.16 ± 0.05	103.76 ± 0.97	44.3 ± 1.8	2.34 ± 0.10	0	14
R2	1.53 ± 0.05	1.90 ± 0.08	0.80 ± 0.04	104.97 ± 1.54	133.4 ± 2.8	0.79 ± 0.02	4	14
R3	1.29 ± 0.06	1.98 ± 0.05	0.65 ± 0.03	100.06 ± 2.07	149.8 ± 1.8	0.67 ± 0.02	8	12
R4	0.43 ± 0.03	0.73 ± 0.04	0.58 ± 0.05	6.26 ± 0.81	26.6 ± 1.2	0.24 ± 0.03	12	9
R5	0.78 ± 0.04	1.92 ± 0.11	0.41 ± 0.03	56.74 ± 1.39	90.0 ± 3.8	0.63 ± 0.03	16	6
R6	1.54 ± 0.05	3.65 ± 0.15	0.42 ± 0.02	78.95 ± 1.45	131.1 ± 4.4	0.60 ± 0.02	18	9
R7	0.71 ± 0.04	1.97 ± 0.14	0.36 ± 0.03	25.72 ± 1.23	93.0 ± 4.4	0.28 ± 0.02	18	14
R8	0.84 ± 0.03	1.80 ± 0.08	0.47 ± 0.03	28.85 ± 1.09	94.4 ± 2.5	0.31 ± 0.01	20	3
R9	1.35 ± 0.03	3.63 ± 0.08	0.37 ± 0.01	108.83 ± 1.11	199.9 ± 2.9	0.54 ± 0.01	16	-1
R10	1.49 ± 0.07	2.20 ± 0.08	0.68 ± 0.04	62.03 ± 1.92	111.0 ± 2.2	0.56 ± 0.02	12	-5
R11	1.49 ± 0.07	1.94 ± 0.03	0.77 ± 0.04	94.26 ± 2.63	172.2 ± 1.1	0.55 ± 0.02	8	-8
R12	1.74 ± 0.06	3.02 ± 0.04	0.57 ± 0.02	112.76 ± 2.01	176.3 ± 1.4	0.64 ± 0.01	4	-10
R13	1.93 ± 0.09	1.66 ± 0.07	1.16 ± 0.07	194.32 ± 3.64	139.4 ± 2.8	1.39 ± 0.04	0	-12
R14	2.46 ± 0.09	3.40 ± 0.03	0.72 ± 0.03	252.08 ± 3.58	192.5 ± 1.3	1.31 ± 0.02	-4	-13
R15	2.68 ± 0.08	3.18 ± 0.09	0.84 ± 0.04	239.52 ± 3.24	374.4 ± 3.4	0.64 ± 0.01	-8	-11
R16	3.46 ± 0.11	4.80 ± 0.18	0.72 ± 0.04	211.39 ± 3.69	301.1 ± 6.0	0.70 ± 0.02	-12	-8
R17	1.67 ± 0.01	1.68 ± 0.06	0.99 ± 0.04	106.98 ± 0.22	141.2 ± 2.3	0.76 ± 0.01	-16	-5
R18	0.79 ± 0.01	2.47 ± 0.07	0.32 ± 0.01	56.68 ± 0.62	159.4 ± 2.8	0.36 ± 0.01	-20	1
R19	1.28 ± 0.05	1.72 ± 0.08	0.75 ± 0.04	49.41 ± 1.41	75.5 ± 2.4	0.65 ± 0.03	-16	6
R20	1.94 ± 0.07	3.19 ± 0.06	0.61 ± 0.02	115.44 ± 2.06	168.9 ± 1.8	0.68 ± 0.01	-12	10
R21	1.83 ± 0.05	1.66 ± 0.06	1.10 ± 0.05	97.04 ± 1.48	81.3 ± 1.8	1.19 ± 0.03	-8	13
R22	1.10 ± 0.04	0.47 ± 0.04	2.32 ± 0.22	62.59 ± 1.26	46.3 ± 1.3	1.35 ± 0.05	-4	14

## 4.2. Molecular Gas Column Density and Mass

Because CO(1–0) traces the bulk of the molecular gas, we can calculate the molecular gas column density and mass from the CO(1–0) integrated intensities. The column density of the molecular hydrogen can be estimated with a conversion factor,  $X_{\text{CO}}$ ,

$$N_{\text{H}_2} = X_{\text{CO}} \int T_{\text{B}}(\text{CO } J = 1 - 0) dv \text{ [cm}^{-2}\text{]}, \quad (1)$$

where  $X_{\text{CO}} \cong 0.4 \times 10^{20} \text{ cm}^{-2} (\text{K km s}^{-1})^{-1}$  for circumnuclear molecular gas (Wilson 1995; Mauersberger et al. 1996; Weiß et al. 2001; Espada et al. 2009) and  $X_{\text{CO}} \cong 3 \times 10^{20} \text{ cm}^{-2} (\text{K km s}^{-1})^{-1}$  for spiral arm regions (Solomon et al. 1987; Young et al. 1991). The column density  $N_{\text{H}_2}$  for each region is calculated using  $\int T_{\text{B}}(\text{CO } J = 1 - 0) dv$  shown in Table 1, and the derived values are shown in Table 2. We also derive the molecular gas mass,  $M_{\text{H}_2}$ , which is displayed in Table 2. The total missing flux of CO(1–0) within the central circular area of 30'' radius is about 35% (Papadopoulos & Seaquist 1999). However, the missing flux is dominated by extended structures, so the true missing fluxes in the core and the compact spiral structures should be smaller. For example, the missing flux of CO(1–0) in the core region is about 20% as discussed in Sect. 3. We thus expect that the errors of the column densities caused by the missing flux are less than 35%.

Table 1—Continued

Area	Peak CO(3–2) [K]	Peak CO(1–0) [K]	Peak $R_{31}$	$\int T_{\text{B}}(\text{CO } J = 3 - 2) dv$ [K km s <sup>−1</sup> ]	$\int T_{\text{B}}(\text{CO } J = 1 - 0) dv$ [K km s <sup>−1</sup> ]	$R_{31}$	X offset [arcsec]	Y offset [arcsec]
R23	$1.02 \pm 0.05$	$2.72 \pm 0.07$	$0.38 \pm 0.02$	$45.12 \pm 1.70$	$94.9 \pm 2.1$	$0.48 \pm 0.02$	-24	-4
R24	$0.96 \pm 0.03$	$2.95 \pm 0.16$	$0.33 \pm 0.02$	$39.06 \pm 0.86$	$126.5 \pm 4.5$	$0.31 \pm 0.01$	-24	-9

Note. — Column (1): Region name. Column (2): Peak brightness temperature of CO(3–2). Column (3): Peak brightness temperature of CO(1–0). Column (4): Line ratio of peak brightness temperature of CO(3–2)/CO(1–0). Column (5): Integrated brightness temperature of CO(3–2). Column (6): Integrated brightness temperature of CO(1–0). Column (7): Line ratio of integrated brightness temperature of CO(3–2)/CO(1–0). The errors Column (8,9): Position offset of region center from the phase center. Errors were estimated from the statistical errors of the spectra; uncertainties of our flux calibration (about 10% for both CO(1–0) and CO(3–2) lines) and missing fluxes are not included.

Table 2. Molecular gas column density and mass, 8  $\mu\text{m}$  dust and  $\text{H}\alpha + [\text{N II}]$  emission, and star formation rate surface density.

Area	$N_{\text{H}_2}$ $\times 10^{21} [\text{cm}^{-2}]$	$M_{\text{H}_2}$ $\times 10^6 [M_{\odot}]$	$f_{8\mu\text{m,dust}}$ $[\text{MJy sr}^{-1}]$	$f_{\text{H}\alpha+[\text{NII}]}$ $\times 10^4 [\text{eps pixel}^{-1}]^{\text{a}}$	$\Sigma_{\text{SFR}}$ $[M_{\odot} \text{ yr}^{-1} \text{ kpc}^{-2}]$
C1	$5.6 \pm 0.3$	$12.3 \pm 0.8$	$1.05 \times 10^4 \pm 6.4$	73.5	$62.4 \pm 0.04$
R1	$13.3 \pm 0.5$	$19.5 \pm 0.8$	$238 \pm 6.4$	1.51	$1.41 \pm 0.04$
R2	$40.0 \pm 0.8$	$58.6 \pm 1.2$	$260 \pm 6.4$	$> 1.87^{\text{b}}$	$1.54 \pm 0.04$
R3	$44.9 \pm 0.5$	$65.8 \pm 0.8$	$337 \pm 6.4$	$> 2.57^{\text{b}}$	$2.00 \pm 0.04$
R4	$8.0 \pm 0.4$	$11.7 \pm 0.5$	$241 \pm 6.4$	2.35	$1.43 \pm 0.04$
R5	$27.0 \pm 1.1$	$39.5 \pm 1.7$	$180 \pm 6.4$	1.08	$1.07 \pm 0.04$
R6	$39.3 \pm 1.3$	$57.6 \pm 1.9$	$166 \pm 6.4$	$> 0.81^{\text{b}}$	$0.98 \pm 0.04$
R7	$27.9 \pm 1.3$	$40.9 \pm 1.9$	$107 \pm 6.4$	— <sup>b</sup>	$0.63 \pm 0.04$
R8	$28.3 \pm 0.8$	$41.5 \pm 1.1$	$89 \pm 6.4$	$> 0.72^{\text{b}}$	$0.52 \pm 0.04$
R9	$60.0 \pm 0.9$	$87.9 \pm 1.3$	$163 \pm 6.4$	$> 0.65^{\text{b}}$	$0.97 \pm 0.04$
R10	$33.3 \pm 0.7$	$48.8 \pm 1.0$	$158 \pm 6.4$	0.77	$0.94 \pm 0.04$
R11	$51.7 \pm 0.3$	$75.7 \pm 0.5$	$174 \pm 6.4$	0.89	$1.03 \pm 0.04$
R12	$52.9 \pm 0.4$	$77.5 \pm 0.6$	$226 \pm 6.4$	0.97	$1.34 \pm 0.04$
R13	$41.8 \pm 0.8$	$61.3 \pm 1.2$	$212 \pm 6.4$	0.76	$1.26 \pm 0.04$
R14	$57.8 \pm 0.4$	$84.6 \pm 0.6$	$236 \pm 6.4$	1.21	$1.40 \pm 0.04$
R15	$112.3 \pm 1.0$	$164.5 \pm 1.5$	$311 \pm 6.4$	2.17	$1.84 \pm 0.04$
R16	$90.3 \pm 1.8$	$132.3 \pm 2.6$	$381 \pm 6.4$	3.49	$2.26 \pm 0.04$
R17	$42.4 \pm 0.7$	$62.1 \pm 1.0$	$345 \pm 6.4$	2.81	$2.05 \pm 0.04$
R18	$47.8 \pm 0.8$	$70.0 \pm 1.2$	$172 \pm 6.4$	0.62	$1.02 \pm 0.04$
R19	$22.7 \pm 0.7$	$33.2 \pm 1.0$	$185 \pm 6.4$	1.15	$1.10 \pm 0.04$
R20	$50.7 \pm 0.6$	$74.2 \pm 0.8$	$207 \pm 6.4$	1.45	$1.23 \pm 0.04$
R21	$24.4 \pm 0.5$	$35.7 \pm 0.8$	$260 \pm 6.4$	1.33	$1.54 \pm 0.04$
R22	$13.9 \pm 0.4$	$20.4 \pm 0.6$	$231 \pm 6.4$	1.37	$1.37 \pm 0.04$
R23	$28.5 \pm 0.6$	$41.7 \pm 0.9$	$123 \pm 6.4$	0.27	$0.73 \pm 0.04$
R24	$38.0 \pm 1.4$	$55.6 \pm 2.0$	$105 \pm 6.4$	0.15	$0.62 \pm 0.04$

Note. — Column (1): Region names. Column (2): Column density. Column (3): Molecular gas mass. Column (4): Average intensity of dust emission. Column (5): Average intensity of  $\text{H}\alpha + [\text{NII}]$  emission. Column (6): Star formation rate surface density.

<sup>a</sup>Image units in electrons per second per pixels (eps pixel<sup>-1</sup>)

<sup>b</sup>These areas do not have complete H $\alpha$  emission information, since these regions are either located at the edge of or outside the *HST* image.

In the spiral arm regions, the box sizes correspond to  $280 \times 350 \text{ pc}^2$ . The average values of  $N_{\text{H}_2}$  and  $M_{\text{H}_2}$  per region are  $39.8 \times 10^{21} \text{ cm}^{-2}$  and  $58.9 \times 10^6 M_{\odot}$ . The standard deviations of  $N_{\text{H}_2}$  and  $M_{\text{H}_2}$  are large inside the spiral arms, with a value of  $24.0 \times 10^{21} \text{ cm}^{-2}$  and  $34.8 \times 10^6 M_{\odot}$ , respectively, indicating that the molecular gas content within the spiral arms varies substantially from region to region. On the other hand,  $N_{\text{H}_2}$  and  $M_{\text{H}_2}$  for the central core C1 are estimated to be  $5.6 \times 10^{21} \text{ cm}^{-2}$  and  $12.3 \times 10^6 M_{\odot}$  (note that the area of C1 is  $\sim 1.5$  times larger than those in the spiral arms). This indicates that the column density and the mass of the central region are much smaller than the average values in the spiral arms. However, we note that the  $R_{31}$  of C1 is very different from those of the spiral arm regions (see Sect. 4.1), and we have used different conversion factors in estimating the mass and column density (Weiß et al. 2001).

Tacconi et al. (1994) and Sternberg, Genzel & Tacconi (1994) showed that the  $N_{\text{H}_2}$  column density in the core region is about  $4 \times 10^{22} \text{ cm}^{-2}$  using the Galactic CO to  $N_{\text{H}_2}$  conversion factor. Our conversion factor for the core region is about  $\frac{1}{6}$  of the Galactic conversion factor and we obtained a  $N_{\text{H}_2}$  column density of  $5.6 \times 10^{21} \text{ cm}^{-2}$ ; in other words, the different results are mainly caused by the different conversion factors adopted. However, we note that a lower conversion factor is typically found in galaxy centers (Wilson 1995; Mauersberger et al. 1996; Weiß et al. 2001; Espada et al. 2009). In particular, the conversion factor in the center of NGC 1068 could be six times lower than the Galactic value (Usero et al. 2004; Garcia-Burillo et al. 2010).

In Figure 5, we compare our CO(3–2) image with the X-ray image obtained with the *Chandra X-ray Observatory* (Young et al. 2001). The X-ray image displays clear emission from the ionization cone emanating from the nucleus of NGC 1068; however, we note that there is an obvious dimmed area at the center of the image. This dimmed area matches well with the central core of our CO(3–2) image, suggesting that the obscuring material of

the X-rays is closely related to the molecular gas.

### 4.3. CO(3–2) Rotation Curve

The rotation curve in the nucleus of NGC 1068 is plotted in Figure 6. The data points and the error bars were derived using the MIRIAD task VELFIT. We ignore points within  $30^\circ$  of the minor axis (P.A. =  $60^\circ$ ), and we assume the inclination angle to be  $45^\circ$  following Schinnerer et al. (2000). Within the central  $2''$  ( $\sim 140$  pc), the rotational velocity increases with radius (rigid rotation). The enclosed mass within the central  $2''$  can be estimated using  $M(r < 2'') \sim rv^2/G$ , and we find that the total mass within this area is  $3.7 \times 10^8 M_\odot$ , which is consistent with Schinnerer et al. (2000). The molecular gas mass in C1 is about  $12.3 \times 10^6 M_\odot$ , so that the gas-to-dynamical mass ratio is 3%. This value is a factor of a few lower than those in star forming galaxies ( $\sim 10\%$ ) (Sakamoto et al. 1999; Koda et al. 2005).

For radii larger than  $2''$ , the rotation curve becomes slowly decreasing. This rotation curve is well fitted with the Brandt rotation curve (Brandt 1960):

$$V = \frac{V_{\max} \frac{R}{R_{\max}}}{\left(\frac{1}{3} + \frac{2}{3} \left(\frac{R}{R_{\max}}\right)^n\right)^{\frac{3}{2n}}} \quad (2)$$

with  $V_{\max} = 116 \text{ km s}^{-1}$ ,  $R_{\max} = 2''.7$ , and  $n = 6$  (Figure 6). The mass from the Brandt model is:

$$M_{\text{tot}} = \left(\frac{3}{2}\right)^{\frac{3}{n}} \frac{V_{\max}^2 R_{\max}}{G}. \quad (3)$$

The total mass inside 190 pc ( $\sim 2.7''$ ) radius is  $7.2 \times 10^8 M_\odot$ .

### 4.4. Relation between CO Line Ratio and Star Formation

As shown in Sect. 4.1,  $R_{31}$  varies along the spiral arms. Since the CO(3–2) line is more closely related to star formation (Komugi et al. 2007), and  $R_{31}$  increases with increasing

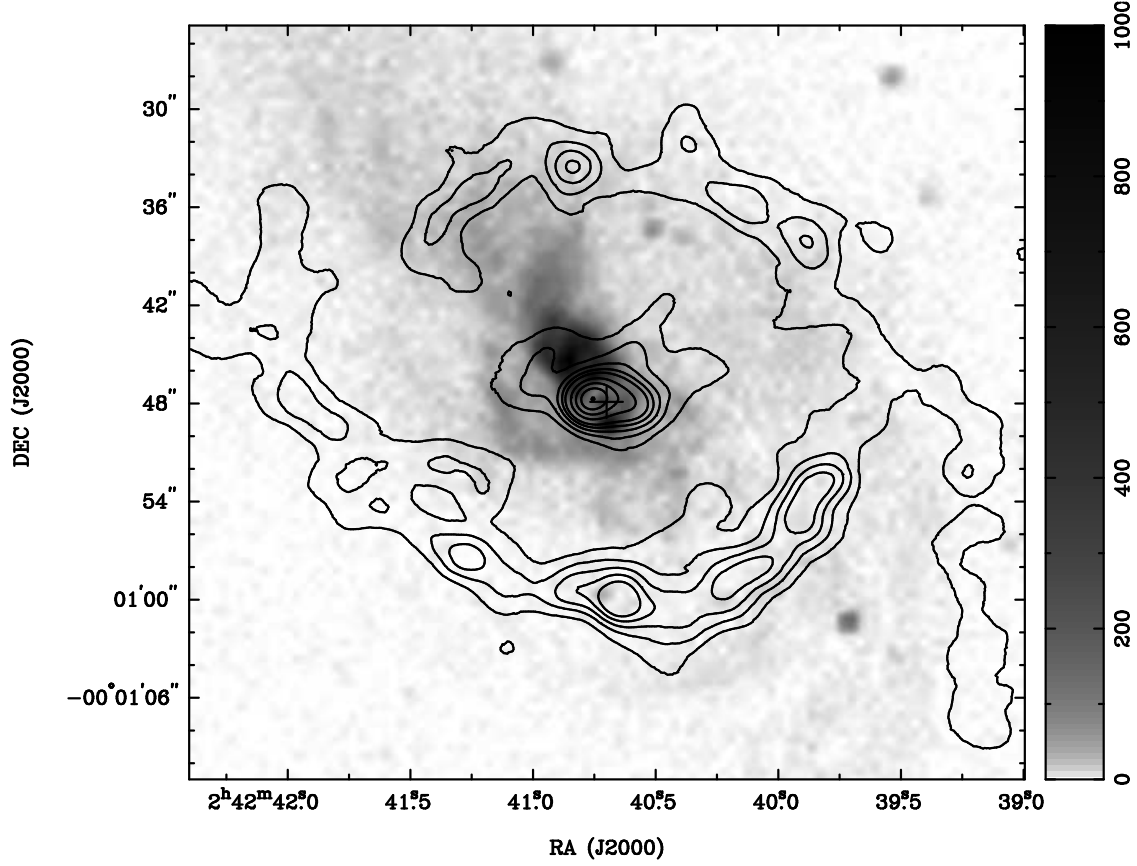


Fig. 5.— Comparison between our CO(3–2) image and the X-ray image taken with the *Chandra X-ray Observatory* (Young et al. 2001). The contours show CO(3–2) emission, with levels 10, 20, 30, 40, 50, 70, 90, 110, and  $130 \times 4.41 \text{ Jy beam}^{-1} \text{ km s}^{-1}$ . The gray scale shows the X-ray emission from 0 to 1000 counts pixel<sup>-1</sup>(0.4 – 5.0 keV).

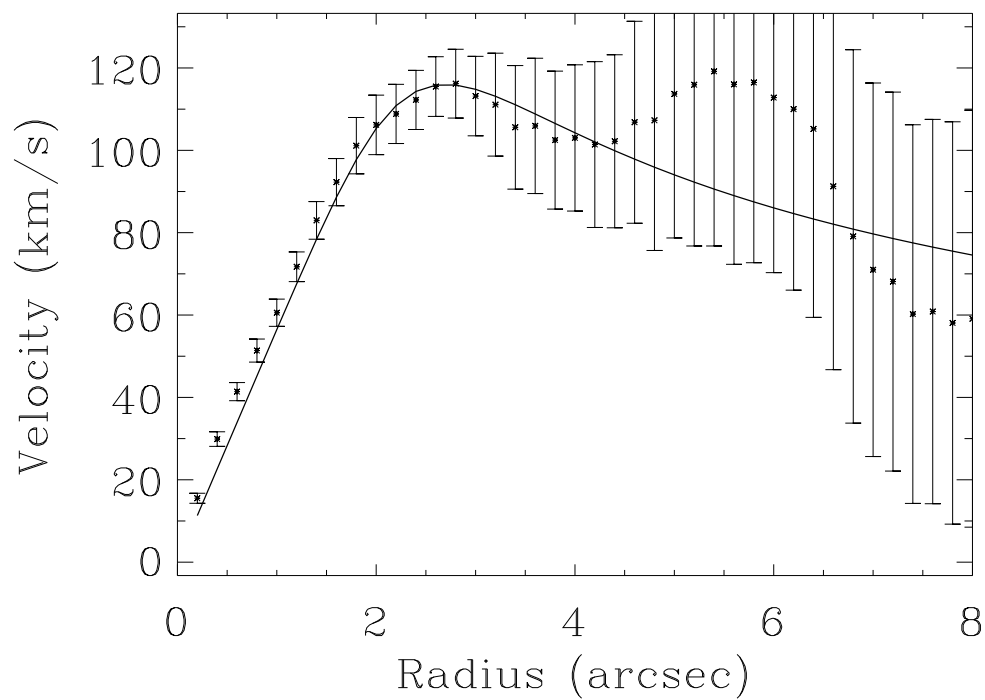


Fig. 6.— Rotation curve of CO(3–2) in the central region of NGC 1068. Crosses with error bars are the data points, and the solid curve is the fitted Brandt rotation curve (see the main text for details).

star formation efficiency (Muraoka et al. 2007), the variation in  $R_{31}$  along the spiral arms of NGC 1068 may also be related to star formation. To study the cause of the variation, we compare  $R_{31}$  with star formation surface density along the spiral arms.

We use both infrared and optical observations as star formation tracers. The infrared data are obtained from the *Spitzer Space Telescope* IRAC 3.6  $\mu\text{m}$  and 8  $\mu\text{m}$  images<sup>3</sup>. Wu et al. (2005) showed that dust emission at 8  $\mu\text{m}$  can be used as a star formation indicator. We estimate the dust emission of in the spiral arms of NGC 1068 using the observed *Spitzer* IRAC 3.6  $\mu\text{m}$  and 8  $\mu\text{m}$  fluxes:

$$f_{8\mu\text{m}}(\text{dust}) = f_{8\mu\text{m}} - \eta_8 f_{3.6\mu\text{m}}, \quad (4)$$

where  $\eta_8 = 0.232$  (Leitherer et al. 1999; Helou et al. 2004). The derived values are shown in Table 2.

H $\alpha$  emission is also considered as a tracer of star formation. For NGC 1068, the wavelength of H $\alpha$  is shifted to 6587.8 Å and those of [N II] to 6573, 6603 Å. To obtain the H $\alpha$  emission, we retrieved the *Hubble Space Telescope (HST)* F658N and F791W images from the STScI archive<sup>4</sup>. The F658N narrow-band filter has a central wavelength of 6590.8 Å with a bandwidth of  $\sim 30$  Å; therefore, the F658N image includes the H $\alpha$  line as well as [N II] lines, which are shifted to 6573 and 6603 Å for NGC 1068. Since this image also includes continuum emission, we correct it using the nearby broad-band filter F791W. The F791W filter has a central wavelength of 7881 Å with a bandwidth of  $\sim 1231$  Å. The continuum subtraction can be performed using the following equation:

$$f_{\text{line}} = \frac{f_{\text{NB}}\Delta\lambda_{\text{BB}} - f_{\text{BB}}\Delta\lambda_{\text{NB}}}{\Delta\lambda_{\text{BB}} - \Delta\lambda_{\text{NB}}}, \quad (5)$$

---

<sup>3</sup><http://ssc.spitzer.caltech.edu/archanaly/archive.html>

<sup>4</sup><http://archive.stsci.edu>

where  $f_{\text{line}}$  is the continuum-subtracted line flux,  $f_{\text{NB}}$  and  $f_{\text{BB}}$  are the observed total fluxes in the narrow-band and broad-band filters, respectively, and  $\Delta\lambda_{\text{NB}}$  and  $\Delta\lambda_{\text{BB}}$  are the bandwidths of the narrow-band and broad-band filters, respectively. The resulting continuum-subtracted F658N image can be considered as the  $\text{H}\alpha + [\text{N II}]$  image. The derived values are shown in Table 2. We cannot separate the  $\text{H}\alpha$  from the  $[\text{N II}]$  lines and we cannot correct the  $\text{H}\alpha + [\text{N II}]$  image for internal extinction with available data. Therefore, we can not obtain any quantitative information from this image; we only use the continuum-subtracted emission as a possible indicator of relative star formation rates.

We compare the *HST*  $\text{H}\alpha + [\text{N II}]$  line intensity with the *Spitzer* 8  $\mu\text{m}$  dust intensity. As can be seen in Figure 7, the  $\text{H}\alpha + [\text{N II}]$  line intensity and the 8  $\mu\text{m}$  dust intensity are linearly correlated, indicating that the former image is effectively also a good star formation tracer. We note that the CO distribution also matches very well with the dust lanes along the spiral arms in the *HST*  $\text{H}\alpha + [\text{N II}]$  line image (Figure 3). The star forming regions are also located along the spiral arms but slightly shifted toward the outside of the spiral arms, especially in the southern spiral arm. This is similar to the results of previous observations for the spiral arms of the nearby galaxy M51 (Vogel et al. 1988; Aalto et al. 1999; Koda et al. 2009).

We also compare molecular gas properties with the star formation rate surface density ( $\Sigma_{\text{SFR}}$ ) derived from the *Spitzer* IRAC 8  $\mu\text{m}$  and 3.6  $\mu\text{m}$  data. The  $\Sigma_{\text{SFR}}$  is derived from the 8  $\mu\text{m}$  dust luminosity:

$$\frac{\Sigma_{\text{SFR}}}{(M_{\odot} \text{ yr}^{-1})} = \frac{\nu L_{\nu}[8\mu\text{m}(\text{dust})]}{1.57 \times 10^9 L_{\odot}} \quad (6)$$

(Wu et al. 2005), where  $L_{\nu}$  is the 8  $\mu\text{m}$  dust luminosity. The derived values are shown in Table 2.

Figure 8 shows the comparison between  $R_{31}$  and  $\Sigma_{\text{SFR}}$  of the spiral arm regions. The correlation coefficient  $r$  between the  $R_{31}$  and  $\Sigma_{\text{SFR}}$  is 0.33 with a probability  $p = 89\%$  of

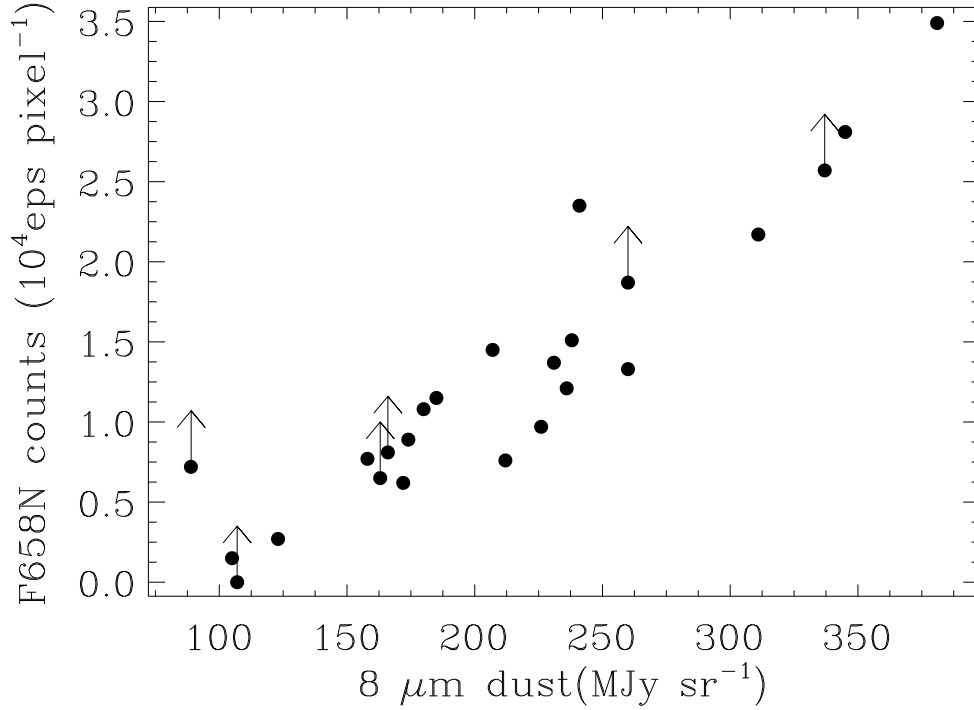


Fig. 7.— Comparison of the *Spitzer* 8  $\mu\text{m}$  dust intensity with the *HST* continuum-subtracted  $\text{H}\alpha + [\text{N II}]$  line intensity. The *HST* line intensity is not flux-calibrated and is expressed in instrument units. The data points with upper arrows do not have complete  $\text{H}\alpha$  emission information because they are located either at the edge of or outside the *HST* image.

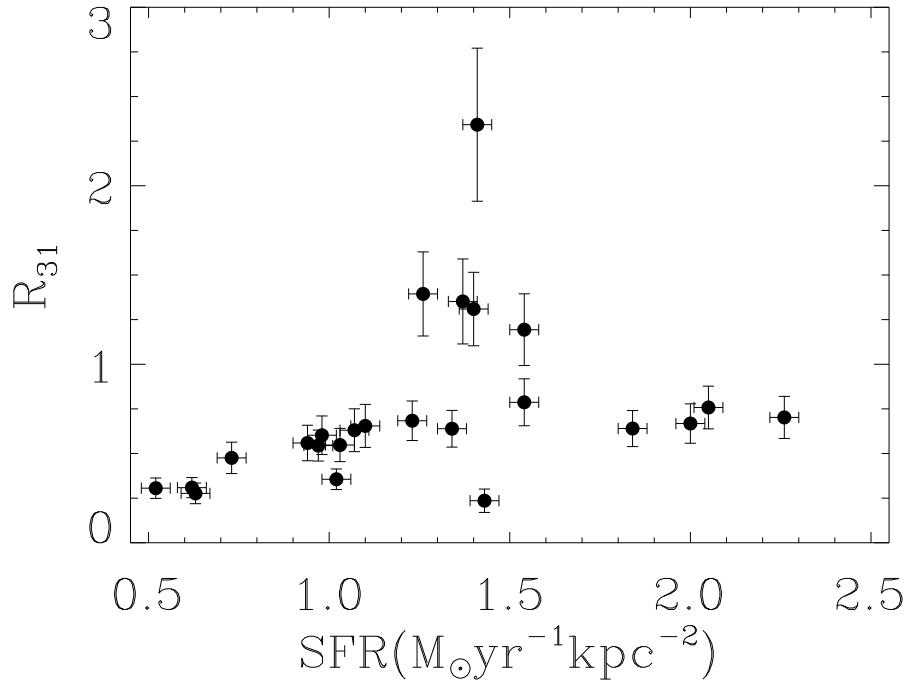


Fig. 8.— Comparison between the CO(3-2)/CO(1-0) integrated intensity ratio,  $R_{31}$ , and the star formation rate surface density ( $\Sigma_{\text{SFR}}$ ). The error bars have included the  $\sim 10\%$  uncertainty of our flux calibrations for the CO(3-2) and CO(1-0) emission.

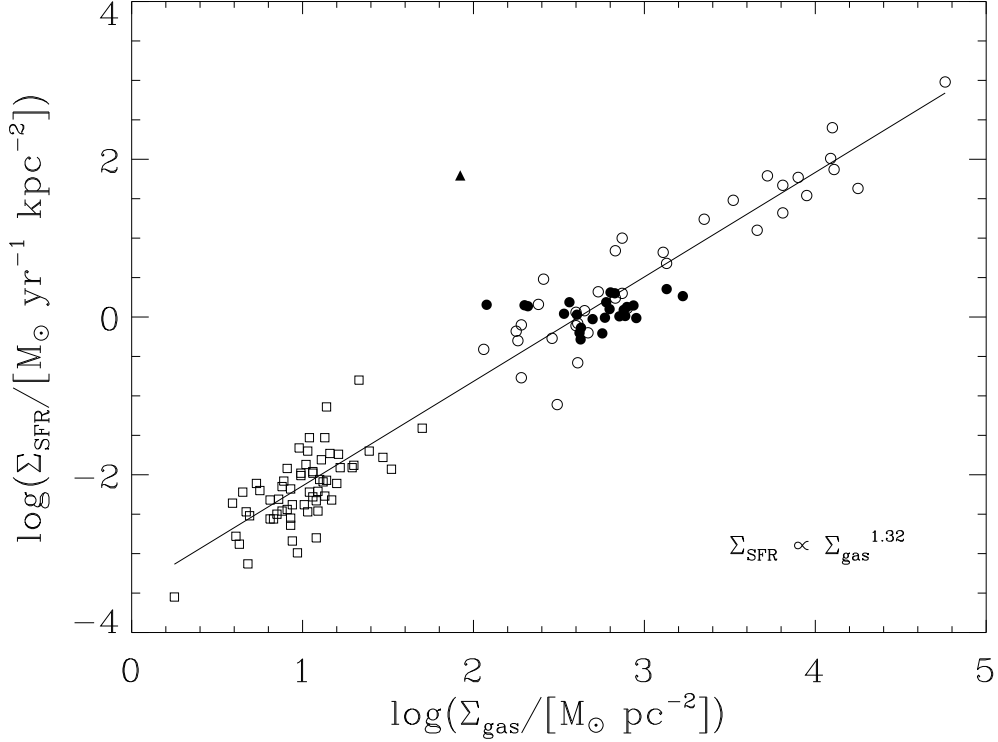


Fig. 9.— Relation between the surface density of molecular gas  $\Sigma_{\text{gas}}$  and  $\Sigma_{\text{SFR}}$  for normal galaxies (open squares), starburst galaxies (open circles), and the spiral arm regions of NGC 1068 (filled circles). The gas surface density is derived from CO(1–0) emission. The normal and starburst galaxy samples are obtained from Kennicutt (1998). The solid triangle is the nuclear region of NGC 1068 (C1). The solid line represents the power-law fit to all data points.

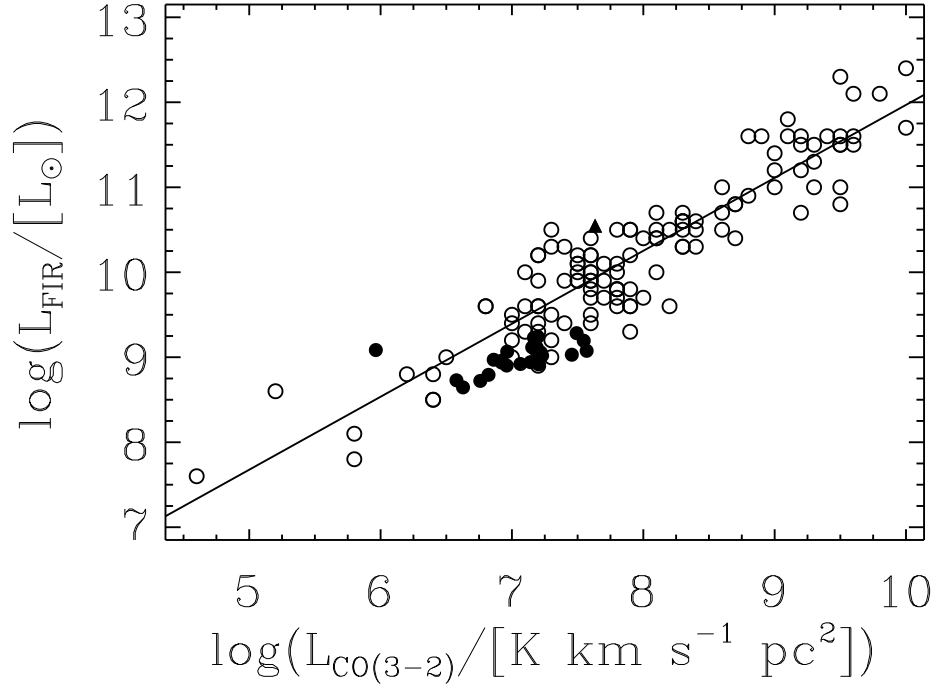


Fig. 10.— Relation between integrated CO(3–2) and FIR luminosities. The filled circles represent the data of the spiral arm regions of NGC 1068, and the solid triangle is the nuclear region of NGC 1068 (C1). The open circles are the data obtained from Mao et al. (2010). The solid line represents the linear fit to all data points. The outlier point with the lowest CO(3–2) emission is R4.

mutual correlation. We note that most of the  $R_{31}$  of nearby star-forming galaxies are within 0.2–0.7 (Mauersberger et al. 1999). For examples, Muraoka et al. (2007) found that the CO emission of the starburst galaxy M83 has  $R_{31} < 1$  and show a good correlation between the  $R_{31}$  and SFE of their data. If we consider the data with  $R_{31} < 1$  in our results, we find that the correlation between the  $R_{31}$  and  $\Sigma_{\text{SFR}}$  becomes highly significant with  $r = 0.63$  and  $p = 99\%$ . This suggests that in normal star-forming regions the physical conditions of molecular gas indicated by  $R_{31}$  are well correlated with dust emission. The data points where  $R_{31} > 1.0$  are obviously out of the correlation, suggesting that the large  $R_{31}$  might be caused by other reasons, such as a different heating mechanism for the molecular gas or different distributions of warm and cool molecular gas (e.g., Ho et al. 1987).

Figure 9 shows the relation between the surface density of molecular gas  $\Sigma_{\text{gas}}$  and  $\Sigma_{\text{SFR}}$ . The star formation rate surface densities of the spiral arm regions of NGC 1068 are much higher than those of normal galaxies and similar to those of starburst galaxies; however, they all seem to follow the same star formation law (Kennicutt 1998). This result strongly supports the idea that the spiral arms in the inner  $\sim 2$  kpc region are experiencing a starburst. On the other hand, the molecular gas at C1 is obviously offset from the Schmidt-Kennicutt law, suggesting that C1 is mainly affected by AGN activities instead of star formation.

In Figure 10, we present the Schmidt-Kennicutt law for the CO(3–2) emission. We used the FIR luminosity instead of the SFR in Figure 9 so that it is easier to compare with the results of Mao et al. (2010). We first derive the star formation rate from the observed  $8\mu\text{m}$  dust luminosity (Wu et al. 2005) and then use the SFR– $L_{\text{FIR}}$  relation,  $\text{SFR}(M_{\odot}\text{yr}^{-1}) \sim 1.7 \times 10^{-10}(L_{\text{FIR}}/L_{\odot})$  (Kennicutt 1998), to derive  $L_{\text{FIR}}$ . We note that this is effectively a Schmidt-Kennicutt law for CO(3–2) emission since  $L_{\text{FIR}}$  is proportional to SFR, and the integrated CO(3–2) luminosity represents the molecular mass in relatively

warm and/or dense regions. We find that most of our results follow the same relation obtained by Mao et al. (2010) for nearby galaxies. The only outlier point, which has the lowest CO(3–2) emission, is the interarm region R4. When we combine our results with Mao et al. (2010), we find that the derived power-law index of the  $L_{CO(3-2)}-L_{FIR}$  relation is  $\sim 0.9$ . This value is smaller than the index of the traditional Schmidt-Kennicutt law, which is around 1.0 to 2.0, but is reasonable for the excitation conditions of warm and/or dense gas (Krumholz & Thompson 2007; Narayanan et al. 2008).

In Figure 9 and Figure 10, the physical scale of the NGC 1068 data is about  $280 \times 350 \text{ pc}^2$ , which is much smaller than those of Kennicutt (1998) and Mao et al. (2010). We note that there is no correlation between  $\Sigma_{\text{gas}}$  and  $\Sigma_{\text{SFR}}$  in Figure 9 when only considering the NGC 1068 data. On the other hand, the CO(3–2) emission from the same NGC 1068 regions show a very good correlation with the infrared as shown in Figure 10; the correlation coefficient  $r$  is 0.789 with a probability  $p = 99.9\%$ . The power-law index of the  $L_{CO(3-2)}-L_{FIR}$  relation for the NGC 1068 data alone (excluding R4) is about 0.49. This value is significantly lower than a typical power-law index of the Schmidt-Kennicutt law.

In Figure 10, the CO(3–2) to FIR luminosity distribution is generally consistent with previous studies, which have a power law index of the Schmidt-Kennicutt law  $\sim 1.0$ . On the other hand, the Schmidt-Kennicutt law derived from the CO(1–0) data has a steeper slope than that from the CO(3–2) data (Figure 9). Furthermore, if we only consider our NGC 1068 data, we find a very flat power law index, which cannot be explained by the model of Krumholz & Thompson (2007) with a different critical density. One possibility is that the gas is under sub-thermal conditions, which would produce a flatter KS law as shown by Narayanan et al. (2008). This interpretation is also consistent with the relatively large line ratios of CO(3–2)/CO(1–0). We also note that most of our data are under the average value of the KS law, indicating that the SFE of the inner spiral regions of NGC 1068 is

smaller than that in most of the sources in Figure 10.

There is also a radial variation of star formation activity in the spiral arm regions. The average star formation rate surface density of the inner arm regions (R1 – R4, R9 – R17, and R19 – R22) is  $1.45 M_{\odot} \text{ yr}^{-1} \text{ kpc}^{-2}$ , and the outer arm regions (R5 – R8, R18, R23, and R24) is  $0.80 M_{\odot} \text{ yr}^{-1} \text{ kpc}^{-2}$ . In other words, the radial variation of the physical conditions of the molecular gas mentioned in Sect. 4.1 is correlated with the radial variation of the galaxy’s star formation.

## 5. SUMMARY

We have shown and compared the emission of different CO rotational transitions of the prototypical Seyfert 2 galaxy NGC 1068 observed with millimeter and submillimeter interferometers. The molecular gas in the central part of this galaxy is distributed in a central core and outer spiral arms. Both the CO(1–0) and CO(3–2) lines show similar distribution along the spiral arms, and most of the molecular gas mass is located in the spiral arms. However, the nucleus is rather different; the strongest CO(3–2) peak lies in the nucleus, but this is not true for CO(1–0). This is very similar to another Seyfert 2 galaxy M51, suggesting that the AGN is playing an important role in the different behaviors of these two CO transition lines.

In the spiral arms, the CO(3–2)/CO(1–0) integrated intensity ratio is well correlated with the star formation rate surface density, indicating that the physical conditions of molecular gas are related to star formation. Both the CO(3–2)/(1–0) ratio and the star formation rate decrease with radius from the nucleus.

The authors thank an anonymous referee for important suggestions. MT and CYH acknowledge support from the National Science Council (NSC) of Taiwan through grant

NSC 100-2119-M-008-011-MY3 and NSC 99-2112-M-008-014-MY3. SM acknowledges support from the NSC of Taiwan through grant NSC 97-2112-M-001-021-MY3. DE was supported by a Marie Curie International Fellowship within the 6<sup>th</sup> European Community Framework Programme (MOIF-CT-2006-40298).

## REFERENCES

- Aalto, S., et al. 1994, *A&A*, 286, 365
- Aalto, S., Huttemeister, S., Scoville, N. Z., Thaddeus, P. 1999, *ApJ*, 522, 165
- Antonucci, R. R. J., & Miller, J. S. 1985, *ApJ*, 297, 621
- Baker, A. J. & Scoville, N. Z. 1998, in *The central regions of the Galaxy and galaxies*,  
Proceedings of the 184th symposium of the International Astronomical Union, ed.  
Y. Sofue (Dordrecht: Kluwer), 221
- Brandt, J. C. 1960, *ApJ*, 131, 293
- Davies, R. I., Sugai, H., & Ward, M. J. 1998, *MNRAS*, 300, 388
- de Vaucouleurs, G., de Vaucouleurs, A., Corwin, H. G., Jr., Buta, R. J., Paturel, G., &  
Fouque, P. 1991, *Third Reference Catalogue of Bright Galaxies* (New York: Springer)
- Devereux, N., Taniguchi, Y., Sanders, D. B., Nakai, N., & Young, J. S. 1994, *AJ*, 107, 2006
- Dumke, M., Nieten, Ch., Thuma, G., Wielebinski, R., & Walsh, W. 2001, *A&A*, 373, 853
- Emsellem, E., Fathi, K., Wozniak, H., Ferruit, P., Mundell, C. G., & Schinnerer, E. 2006,  
*MNRAS*, 365, 367
- Espada, D., Matsushita, S., Peck, A., Henkel, C., Iono, D., Israel, F. P., Muller, S., Petitpas,  
G., Pihlstrom, Y., Taylor, G. B., Dinh-V-Trung 2009, *ApJ*, 695, 116
- Gallimore, J. F., Baum, S. A., & O’Dea, C. P. 1997, *Nature*, 388, 852
- Gallimore, J. F., Baum, S. A., & O’Dea, C. P. 2004, *ApJ*, 613, 794
- Gallimore, J. F., Baum, S. A., O’Dea, C. P., & Pedlar, A. 1996, *ApJ*, 458, 136

- Gallimore, J. F., Henkel, C., Baum, S. A., Glass, I. S., Claussen, M. J., Prieto, M. A., & Von Kap-herr, A. 2001, *ApJ*, 556, 694
- Gao, Y., & Solomon, P. M. 2004, *ApJS*, 152, 63
- Garcia-Burillo, S., et al. 2010, *A&A*, 519, A2
- Greenhill, L. J., Gwinn, C. R., Antonucci, R., & Barvainis, R. 1996, *ApJ*, 472, L21
- Helfer, T. T., & Blitz, L. 1995, *ApJ*, 450, 90
- Helfer, T. T., Thornley, M. D., Regan, M. W., Wong, T., Sheth, K., Vogel, S. N., Blitz, L., & Bock, D. C.-J. 2003, *ApJS*, 145, 259
- Helou, G., et al. 2004, *ApJS*, 154, 253
- Ho, P.T.P, Turner, J. L., & Martin, R. N. 1987, *ApJ*, 322, L67
- Hsieh, P.-Y., Matsushita, S., Lim, J., Kohno, K., & Sawada-Satoh, S. 2008, *ApJ*, 683, 70
- Huré, J.-M. 2002, *A&A*, 395, L21
- Israel, F. P. 2009, *A&A*, 493, 525
- Jackson, J. M., Paglione, T. A. D., Ishizuki, S., & Nguyen-Q-Rieu 1993, *ApJ*, 418, L13
- Jaffe, W., et al. 2004, *Nature*, 429, 47
- Kaneko, N., Morita, K., Fukui, Y., Sugitani, K., Iwata, T., Nakai, N., & Kaifu, N. 1989, *ApJ*, 337, 691
- Kaneko, N., Morita, K., Fukui, Y., Takahashi, N., Sugitani, K., Nakai, N., & Morita, K.-I. 1992, *PASJ*, 44, 341
- Kennicutt, R. C. 1998, *ApJ*, 498, 541

- Kennicutt, Jr., R. C., Calzetti, D., Walter, F., et al. 2007, *ApJ*, 671, 333
- Koda, J., Okuda, T., Nakanishi, K., Kohno, K., Ishizuki, S., Kuno, N., & Okumura, S. K. 2005, *A&A*, 431, 887
- Koda, J., Scoville, N., Sawada, T., et al. 2009, *ApJ*, 700, 132
- Kohno, K., et al. 2001, *ASP Conf. Ser.* 249, 672
- Kohno, K. 2005, *AIP Conf. Proc.* 783, 203
- Kohno, K., et al. 2008, *Ap&SS*313, 279
- Komugi, S., Kohno, K., Tosaki, T., Nakanishi, H., Onodera, S., Egusa, F., & Sofue, Y. 2007, *PASJ*, 59, 55
- Krips, M., Neri, R., Garcia-Burillo, S., Martin, S., Combes, F., Gracia-Carpio, J., Eckart, A. 2008 *ApJ*, 677,262
- Krips, M., Martin, S., Eckart, A., Neri, R., Garcia-Burillo, S., Matsushita, S., Peck, A., Stoklasova, I., Petitpas, G., Usero, A., Combes, F., Schinnerer, E., Humphreys, E., & Baker, A. J. 2011, 736, 37
- Krumholz, M. R. & Thompson, T. A. 2007, *ApJ*, 669, 289
- Leitherer, C., et al. 1999, *ApJS*, 123, 3
- Lodato, G., & Bertin, G. 2003, *A&A*, 398, 517
- Macchetto, F., Capetti, A., Sparks, W. B., Axon, D. J., & Boksenberg, A. 1994, *ApJ*, 435, L15
- Maloney, P. R., Hollenbach, D. J., & Tielens, A. G. G. M. 1996, *ApJ*, 466, 561

- Mao, R.-Q., Schulz, A., Henkel, C., Mauersberger, R., Muders, D., & Dinh-V-Trung 2010, ApJ, 724, 1336
- Matsushita, S., et al. 2004, ApJ, 616, L55
- Matsushita, S., Muller, S., & Lim, J. 2007, A&A, 468, L49
- Matsushita, S., et al. 2009, ApJ, 693, 56
- Matsushita, S., Kawabe, R., Kohno, K., Tosaki, T., & Vila-Vilaró, B. 2010, PASJ, 62, 409
- Matt, G., et al. 1997, A&A, 325, L13
- Mauersberger, R., Henkel, C., Wielebinski, R., Wiklind, T., Reuter, H.-P. 1995, A&A, 305, 421
- Mauersberger, R., Henkel, C., Walsh, W., & Schulz, A. 1999, A&A, 341, 256
- Meijerink, R., & Spaans, M. 2005, A&A, 436, 397
- Meijerink, R., Spaans, M., & Israel, F. P. 2007, A&A, 461, 793
- Mulchaey, J. S., Myshotzky, R. F., & Weaver, K. A. 1992, ApJ, 390, L69
- Müller Sánchez, F., Davies, R. I., Genzel, R., Tacconi, L. J., Eisenhauer, F., Hicks, E. K. S., Friedrich, S., & Sternberg, A. 2009, ApJ, 691, 749
- Muehleman, D. O. & Berge, G. L. 1991, Icarus, 92, 263
- Muraoka, K. et al. 2007, PASJ, 59, 43
- Muxlow, T. W. B., Pedlar, A., Holloway, A. J., Gallimore, J. F., & Antonucci, R. R. J. 1996, MNRAS, 278, 854
- Myers, S. T., & Scoville, N. Z. 1987, ApJ, 312, L39

- Narayanan, D., Cox, T. J., Shirley, Y., Davé, R., Hernquist, L., Walker, C. K. 2008a, *ApJ*, 684, 996
- Oka, T., Nagai, M., Kamegai, K., Tanaka, K., & Kuboi, N. 2007, *PASJ*, 59, 15
- Orton, G. S., Griffin, M. J., Ade, P. A. R., Nolt, I. G., Radostitz, J. V., Robson, E. I., & Gear, W. K. 1986, *Icarus*, 67, 289
- Padin, S., Scott, S. L., Woody, D. P., Scoville, N. Z., Seling, T. V., Finch, R. P., Giovanine, C. J., & Lawrence, R. P. 1991, *PASP*, 103, 461
- Padin, S., et al. 1993, *IEEE Transactions on Instrumentation and Measurement*, 42, 793
- Paglione, T. A. D., et al. 2001, *ApJS*, 135, 183
- Papadopoulos, P. P., & Seaquist, E. R. 1999, *ApJ*, 516, 114
- Pérez-Beaupuits, J. P., Spaans, M., van der Tak, F. F. S., Aalto, S., Garcia-Burillo, S., Fuente, A., Usero, A. 2009, *A&A*, 503, 459
- Petitpas, G. R., & Wilson, C. D. 2000, *ApJ*, 538, L117
- Planesas, P., Gómez-González, J. & Martín-Pintado, J. 1989, *A&A*, 216, 1
- Planesas, P., Scoville, N., & Myers, S. T. 1991, *ApJ*, 369, 364
- Pogge, R. W. 1988, *ApJ*, 328, 519
- Sakamoto, S. 1994, *PASP*, 106, 1112
- Sakamoto, S., Hasegawa, T., Handa, T., Hayashi, M., & Oka, T. 1997, *ApJ*, 486, 276
- Sakamoto, K., Okumura, S. K., Ishizuki, S., & Scoville, N. Z. 1999, *ApJ*, 525, 691
- Sakamoto, K., Ho, P. T. P., Mao, R.-Q., Matsushita, S., & Peck, A. B. 2007, *ApJ*, 654, 782

- Schinnerer, E., Eckart, A., Tacconi, L. J., Genzel, R., & Downes, D. 2000, *ApJ*, 533, 850
- Schmidt, M., 1959, *ApJ*, 129, 243
- Scott, S. L. & Finch, R. P. 1992, in *Proceedings of a Workshop on Remote Observing*, eds. D. T. Emerson & R. G. Clowes (Singapore: World Scientific), 93
- Scoville, N. Z., Young, J. S. & Lucy, L.B. 1983, *ApJ*, 270, 443
- Scoville, N. Z., Matthews, K., Carico, D. P., & Sanders, D. B. 1988, *ApJ*, 327, L61
- Scoville, N. Z., Yun, M. S., Clemens, D. P., Sanders, D. B., & Waller, W. H. 1987, *ApJS*, 63, 821
- Scoville, N. Z., Carlstrom, J. E., Chandler, C. J., Phillips, J. A., Scott, S. L., Tilanus, R. P. J., & Wang, Z. 1993, *PASP*, 105, 1482
- Shepherd, M. C. 1997, in *Astronomical Data Analysis Software and Systems VI*, eds. G. Hunt & H. E. Payne (San Francisco: ASP), 77
- Solomon, P. M., Rivilo, A. R., Barrett, J., & Yahil, A. 1987, *ApJ*, 319, 730
- Sternberg, A., Genzel, R., & Tacconi, L. 1994, *ApJ*, 436, L131
- Tacconi, L. J., Genzel, R., Bleitz, M., Cameron, M., Harris, A. I., & Madden, S. 1994, *ApJ*, 426, L77
- Tan, J. C., 2000, *ApJ*, 536, 173
- Telesco, C. M., Becklin, E. E., Wynn-Williams, C. G., & Harper, D. A. 1984, *ApJ*, 282, 427
- Telesco, C. M., & Decher, R. 1988, *ApJ*, 334, 573
- Thronson, H. A., Jr., et al. 1989, *ApJ*, 343, 158

- Tosaki, T., Shioya, Y., Kuno, N., Hasegawa, T., Nakanishi, K., Matsushita, S., & Kohno, K. 2007, PASJ, 59, 33
- Tully, R. B. 1988, *Nearby Galaxies Catalog* (Cambridge: Cambridge Univ. Press)
- Turner, B. E., 1993, ApJ, 411, 219
- Usero, A., García-Burillo, S., Fuente, A., Martín-Pintado, J., & Rodríguez-Fernández, N. J. 2004, A&A, 419, 897
- Vogel, S. N., Kulkarni, S. R., & Scoville, N. Z. 1988, *Nature*, 334, 402
- Wei, A., Neininger, N., Huttemeister, S., Klein, U. 2001, A&A, 365, 571
- Wilson, C. D. 1995, ApJ, 448, L97
- Wilson, A. S., & Ulvestad, J. S. 1983, ApJ, 275, 8
- Wu, H., Cao, C., Hao, C.-N., Liu, F.-S., Wang, J.-L., Xia, X.-Y., Deng, Z.-G., & Young, C. K.-S. 2005, ApJ, 632, L79
- Young, J. S. & Scoville, N. Z. 1991, ARA&A, 29, 581
- Young, J. S. et al. 1995, ApJS, 98, 219
- Young, A. J., Wilson, A. S., & Shopbell, P. L. 2001, ApJ, 556, 6